Searching for topological density-wave insulators in multiorbital square-lattice systems

Bohm-Jung Yang[1] and Hae-Young Kee[1,2,*]
[1]*Department of Physics, University of Toronto, Toronto, Ontario, Canada M5S 1A7*
[2]*Quantum Materials Program, Canadian Institute for Advanced Research, Toronto, Ontario, Canada M5G 1Z8*
(Received 24 July 2010; published 19 November 2010)

We study topological properties of density-wave states with broken translational symmetry in two-dimensional multiorbital systems with particular focus on t_{2g} orbitals in a square lattice. Due to the distinct symmetry properties of *d*-orbitals, a nodal charge or spin-density-wave state with Dirac points protected by lattice symmetries can be achieved. When an additional order parameter with opposite reflection symmetry is introduced to a nodal density-wave state, the system can be fully gapped leading to a band insulator. Among those, topological density-wave insulators can be realized when an effective staggered on-site potential generates a gap to a pair of Dirac points connected by inversion symmetry which have the same topological winding numbers. We also present a mean-field phase diagram for various density-wave states and discuss the experimental implications of our results.

DOI: 10.1103/PhysRevB.82.195126 PACS number(s): 71.30.+h, 71.27.+a, 71.10.Fd

I. INTRODUCTION

Identifying topological insulators has been one of the most fascinating research fields in contemporary condensed matter physics.[1–3] Topological insulators have a bulk gaplike band insulators but are distinguished by topologically protected conducting edge states preserving time-reversal invariance. In particular, two-dimensional (2D) topological insulators are known as quantum spin Hall insulators with finite spin currents on the edge, analogous to quantum Hall states. Haldane[4] proposed that the fictitious magnetic fluxes in the honeycomb lattice lead to the quantum anomalous Hall insulator (or Chern insulator). Generalizing Haldane's model including time-reversal invariant spin-orbit coupling, it was theoretically shown that such a quantum spin Hall insulator can exist in graphene.[5,6] A two-dimensional semiconductor system with a uniform strain gradient was also proposed to be a candidate.[7] Later, the predicted edge states in HgCeTe quantum well systems[8] were experimentally verified which confirmed the existence of two-dimensional topological insulators.[9]

The topological insulators in these systems normally exist due to strong spin- orbit coupling.[5,10] When the spin-orbit coupling preserves spin rotational symmetry about an axis, the counterpropagating edge modes which carry opposite spin quantum numbers result in quantum spin Hall insulators. It was shown that these modes are protected by time-reversal symmetry even in the absence of spin rotational invariance.[10] It was further pointed out that an effective spin-orbit coupling term can be generated by spontaneous spin rotational symmetry breaking in an extended Hubbard model on the honeycomb lattice.[11] In these studies, the structure of the honeycomb lattice plays an important role, as the tight-binding model on this lattice possesses two Dirac points at the Brillouin-zone corners. Therefore in low-energy description, various gapped insulating phases proximate to the Dirac semimetal can be understood in terms of mass perturbations to gapless Dirac particles. For instance, the fictitious magnetic fluxes introduced by Haldane generate a mass term that has the opposite signs at the two Dirac points leading to an insulator with finite quantized Hall conductivity. The Dirac Hamiltonian approach further provides a framework to understand the time-reversal invariant Z_2 topological insulators.[10]

While systems on the honeycomb lattice such as graphene naturally support two-dimensional massless Dirac particles in the bare band structures, this is not the case in a simple square lattice system which is an effective model for abundant layered perovskite materials in nature. In this respect, it is interesting to note that the recently proposed nodal density-wave state[12] exhibits gapless Dirac particles via broken translational symmetry. This proposal was made in the context of iron pnictide systems, where *d* orbitals of t_{2g} bands in an effectively two-dimensional square lattice give rise to several Fermi pockets with interesting topological properties. In this system, the spin-density-wave instability with the finite ordering wave vector $\mathbf{Q}=(\pi,0)$ [or $(0,\pi)$] leads to band touchings between the $\mathbf{k}$ states with the momentum difference of $\mathbf{Q}$. In general, the degeneracies at the band touching points disappear because of the finite overlap matrix between the degenerate states induced by the density-wave order parameter. However, in multiorbital systems, because of the distinct symmetry properties of orbitals, the degeneracies at some band touching points are protected leading to nodal density-wave states, which is generally valid for any density-wave orders.

In this work, we ask if topological insulators can emerge by gapping nodal points turning the system from nodal density-wave states to topological density-wave (TDW) insulators. To find such a TDW insulator, we first investigate the properties of the nodal density-wave states. We find that one general and important characteristic of the Dirac particles in nodal density-wave states is that a pair of Dirac Hamiltonians connected by inversion symmetry have the same topological winding numbers. Thus an effective staggered on-site potential generating a mass term, which has the same signs at the inversion symmetric nodal points, induces TDW insulators. This can be contrasted with the topological properties of the Dirac particles in the honeycomb lattice where the Dirac Hamiltonians at the two inversion symmetric nodal points have the opposite winding directions.[3,13]

Thus the mass term induced by, for example, a staggered sublattice chemical potential, which has the same signs at the two Dirac points would generate a topologically trivial band insulator as shown in graphene system.[5,14]

The rest of the paper is organized as follows. In Sec. II, we first consider a simple two-band model Hamiltonian composed of d_{xz} and d_{yz} orbitals on the square lattice. After classifying all possible charge and spin-density-wave (SDW) order parameters with the ordering wave vector $\mathbf{Q}=(\pi,0)$ based on their transformation properties under lattice symmetries, we establish general relations between the locations of Dirac nodes and order-parameter symmetries in Sec. III. The fact that d_{xz} and d_{yz} orbitals have the opposite eigenvalues under reflection symmetries along high-symmetry directions in the momentum space plays the key role for the emergence of Dirac points. In addition to the Dirac points coming from the Brillouin-zone folding, additional contributions from quadratic band degeneracy splitting are also discussed. In Sec. IV, topological properties of gapped density-wave phases with two order parameters with the opposite reflection symmetries are studied. Fully gapped insulating phases can be obtained by introducing two density-wave order parameters which have the opposite eigenvalues under reflection symmetries. Among them, a certain combination turns the system to a TDW insulator. In Sec. V, the mean-field phase diagram including the TDW phase is presented, which is obtained by solving an extended Hubbard model Hamiltonian with orbital degeneracy. Topological density-wave states in three orbital systems are discussed in Sec. VI. Straightforward extension to three-orbital systems shows the general applicability of the idea we pursue in this work to obtain topological insulators in multiorbital systems. Finally, we conclude in Sec. VII.

II. TWO-BAND HAMILTONIAN AND SYMMETRIES OF ORDER- PARAMETERS

A. Tight-binding Hamiltonian

We consider a tight-binding Hamiltonian on the square lattice with two orbital (d_{xz},d_{yz}) degrees of freedom at each site. A generic Hamiltonian which contains all possible hopping processes allowed by lattice symmetries is given by

$$H_0=\sum_{\mathbf{k},\sigma}\psi^{\dagger}_{\mathbf{k},\sigma}H(\mathbf{k})\psi_{\mathbf{k},\sigma}, \tag{1}$$

where

$$H(\mathbf{k})=[\varepsilon_+(\mathbf{k})-\mu]\tau_0+\varepsilon_-(\mathbf{k})\tau_3+\varepsilon_{xy}(\mathbf{k})\tau_1. \tag{2}$$

Here a two-component field $\psi^{\dagger}_{\mathbf{k},\sigma}=[d^{\dagger}_{xz,\sigma}(\mathbf{k}),d^{\dagger}_{yz,\sigma}(\mathbf{k})]$ describes the creation of particles with d_{xz} and d_{yz} orbital flavors and spin σ, and the Pauli matrix τ_i connects these two orbital states. In the above,

$$\varepsilon_+(\mathbf{k})=-(t_1+t_2)(\cos k_x+\cos k_y)-4t_3\cos k_x\cos k_y,$$

$$\varepsilon_-(\mathbf{k})=-(t_1-t_2)(\cos k_x-\cos k_y),$$

$$\varepsilon_{xy}(\mathbf{k})=-4t_4\sin k_x\sin k_y. \tag{3}$$

Diagonalization of $H(\mathbf{k})$ gives rise to the following two band dispersions:

$$E_{\pm}(\mathbf{k})=\varepsilon_+(\mathbf{k})-\mu\pm\sqrt{\varepsilon^2_-(\mathbf{k})+\varepsilon^2_{xy}(\mathbf{k})}. \tag{4}$$

In addition to time-reversal symmetry T, the Hamiltonian H_0 has the C_4 point-group symmetry, which consists of the fourfold rotation $C_{\pi/2}$, the inversion I, and the two reflections P_x and P_y mapping x to $-x$ and y to $-y$, respectively. Each symmetry operation transforms a two-component field $\psi_\sigma(k_x,k_y)$ in the following way:

$$C_{\pi/2}:\psi_\sigma(k_x,k_y)\rightarrow i\tau_2\psi_\sigma(-k_y,k_x),$$

$$P_x:\psi_\sigma(k_x,k_y)\rightarrow-\tau_3\psi_\sigma(-k_x,k_y),$$

$$P_y:\psi_\sigma(k_x,k_y)\rightarrow\tau_3\psi_\sigma(k_x,-k_y),$$

$$I:\psi_\sigma(k_x,k_y)\rightarrow-\tau_0\psi_\sigma(-k_x,-k_y). \tag{5}$$

If we choose the hopping parameters in such a way as $t_1=-1.0$, $t_2=1.3$, and $t_3=t_4=-0.85$, the H_0 works as an effective two-band Hamiltonian describing the Fe-pnictide systems.[15] Given the hopping parameters above, the Fermi surface consists of two hole and two electron pockets when the system is near half-filling.[12,15] A pair of electron and hole pockets are connected by a nesting wave vector $\mathbf{Q}=(\pi,0)$ [or $(0,\pi)$], which drives various density-wave instabilities.[16] Here we choose $\mathbf{Q}=(\pi,0)$ (Ref. 17) and perform a detailed study about the band structures of density-wave ground states considering all possible density-wave order parameters.

B. Symmetry of order parameters

We consider various on-site density-wave order parameters and investigate their symmetry properties. Since we have two orbitals per site, there are four different on-site charge-density-wave (CDW) states with the ordering wave vector $\mathbf{Q}=(\pi,0)$, which are given by

$$\hat{D}_i=\frac{1}{N}\sum_{\mathbf{k}}\sum_{a,b=1}^{2}d^{\dagger}_{a,\sigma}(\mathbf{k})[\tau_i]_{ab}d_{b,\sigma}(\mathbf{k}+\mathbf{Q}), \tag{6}$$

where a are b are indices describing the $d_{xz}(a=1)$ or $d_{yz}(a=2)$ orbital states. N counts the number of unit cells in the system. Similarly, we also define SDW states choosing the spin ordering direction along the z axis,

$$\hat{M}_i=\frac{1}{N}\sum_{\mathbf{k}}\sum_{a,b=1}^{2}d^{\dagger}_{a,\sigma_1}(\mathbf{k})[\tau_i]_{ab}[s^z]_{\sigma_1\sigma_2}d_{b,\sigma_2}(\mathbf{k}+\mathbf{Q}). \tag{7}$$

These eight order parameters represent distinct phases with different broken symmetries. For example, the D_3 CDW order parameter corresponds to $\Sigma_i(-1)^{i_x}(n_{i,xz}-n_{i,yz})$, where $n_{i,a}$ is the density of electrons with the orbital a at the site i. Thus it is characterized by the relative density difference between two orbitals (orbital ordering), which alternates along the x direction, while keeping the total density $(n_{i,xz}+n_{i,yz})$ uniform on every site as shown in Fig. 1(a). This

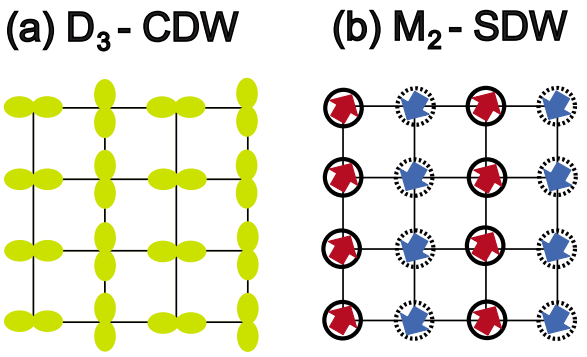

FIG. 1. (Color online) Description of representative density-wave ordering patterns with the ordering wave vector $\mathbf{Q}=(\pi,0)$. (a) D_3 charge-density-wave (D_3-CDW) ordering. d_{xz} and d_{yz} orbitals align alternatively along the x direction while local charge and spin densities are uniform. (b) M_2 spin-density-wave (M_2-SDW) ordering. Here orbital and spin orderings occur at the same time. A solid circle represents the d_+ orbital defined as $d_+=(d_{xz}+id_{yz})/\sqrt{2}$, while a dotted circle indicates the d_- orbital given by $d_-=(d_{xz}-id_{yz})/\sqrt{2}$. The arrows inside circles describe spin ordering.

breaks translational symmetry, doubling the unit cell along x direction. On the other hand, the M_2 SDW order parameter described in Fig. 1(b) corresponds to a staggered spin-orbit coupling. This is because M_2 can be written as $\Sigma_i(-1)^{i_x}S_{i,z}L_{i,z}$, where $L_{i,z}$ is proportional to $(d_{i,xz}+id_{i,yz})^\dagger(d_{i,xz}+id_{i,yz})-(d_{i,xz}-id_{i,yz})^\dagger(d_{i,xz}-id_{i,yz})=2id^\dagger_{i,xz}d_{i,yz}+\text{H.c.}$. However, unlike the uniform spin-orbital coupling $\Sigma_i S_{i,z}L_{i,z}$, the M_2 is a staggered spin-orbit coupling with alternating signs along the x direction. It breaks spin-rotational and translational symmetries but preserves time-reversal symmetry. In addition, D_0 and M_0 describe conventional charge- and spin-density-wave states, respectively. It was found that M_0 describes the leading density-wave instability in Fe-pnictides.[12]

The above eight order parameters can be distinguished by their transformation properties under lattice symmetries. The symmetries of density-wave order parameters are summarized in Table I. Note that every density-wave state has even parity under the inversion symmetry. Moreover, all the diagonal density-wave states D_i (or M_i) with $i=0$ or 3 are even under the two reflection symmetries while the other off-diagonal density-wave states with $i=1$ or 2 are odd under the reflections. These symmetry properties of density-wave order parameters strongly constrain the location of Dirac nodes generated by the Brillouin-zone folding and the winding numbers around Dirac nodes in the momentum space, which are discussed in detail in the following section.

III. NODAL DENSITY-WAVE PHASES

One intriguing property of the $\mathbf{Q}=(\pi,0)$ density-wave ground states is that a large number of Dirac nodes emerge in the band structure.[12] The numbers and locations of the nodal points depend on band dispersions and the symmetries of the order parameters.

There are two different sources generating nodal points in general. One way is via introducing a density-wave order parameter carrying a finite momentum. This induces a Brillouin-zone folding which generates several band touching points. In most cases, the degeneracy at the band touching point is lifted because the density-wave order parameter induces a finite overlap between the pair of states touching at a point. Henceforth a band gap opens up. However, when the band touching occurs at a high-symmetry point in the Brillouin zone, the overlap matrix vanishes due to the lattice symmetries, generating symmetry protected nodal points.

The second group of nodal points come from the splitting of quadratic band touching points, which exist in the bare band structure. Because of the underlying fourfold rotational symmetry, the original hopping Hamiltonian in Eq. (1) supports quadratic band crossing points.[12,18–21] The introduction of the density-wave order parameter carrying a finite momentum splits a quadratic band touching point into two Dirac points along high-symmetry directions in the momentum space. In the following, we discuss in detail the relation between the order-parameter symmetry and the locations of Dirac points derived from these two different sources in separate subsections.

A. Dirac nodes generated by Brillouin-zone folding

We first focus on the generation of Dirac nodes along the k_y axis. In Fig. 2(a) [Fig. 2(b), we plot the energy dispersion of the two bands given in Eq. (4) along the $k_x=0(k_x=\pi)$ direction. Since the ε_{xy} term in Eq. (3), which describes the hybridization between d_{xz} and d_{yz} orbitals, vanishes along the $k_x=0$ axis, the upper and lower bands in Fig. 2(a) are just d_{yz} and d_{xz} bands, respectively. For $k_x=0$, $H(\mathbf{k})$ is invariant under the P_x reflection which transforms a momentum k_x to $-k_x$. Therefore each band is an eigenstate of P_x with eigenvalues of ±1. This is consistent with the fact that $d_{xz}(d_{yz})$ orbital is odd (even) under P_x. A similar analysis can also be applied to the two bands dispersing along the $k_x=\pi$ direction. Since $H(\mathbf{k})$ has P_x symmetry along $k_x=\pi$, the two bands also have definite P_x eigenvalues. In Fig. 2, the P_x even (odd) bands are represented by blue dotted (red solid) lines.

TABLE I. Symmetry of density-wave order parameters. Here "+" ("−") indicates "even" ("odd") symmetry of the order parameters under the corresponding symmetry operation.

	D_0	D_1	D_2	D_3	M_0	M_1	M_2	M_3
P_x	+	−	−	+	+	−	−	+
P_y	+	−	−	+	+	−	−	+
I	+	+	+	+	+	+	+	+
T	+	+	−	+	−	−	+	−

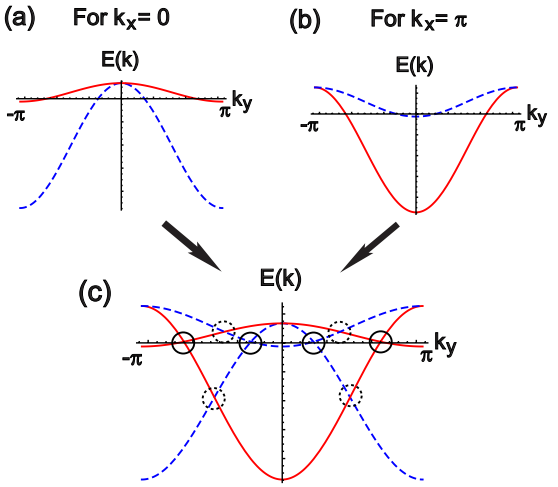

FIG. 2. (Color online) (a) Band dispersion along $k_x=0$ for the hopping Hamiltonian in Eq. (1). Here we use a red solid (blue dotted) line to indicate a band which is odd (even) under the P_x reflection symmetry. (b) Band dispersion along the $k_x=\pi$ direction. (c) Band structure along $k_x=0$ after the unit-cell doubling due to the $\mathbf{Q}=(\pi,0)$ density-wave ordering. Four bands in (a) and (b) meet and disperse together along $k_x=0$ after the Brillouin-zone folding. Note that the zone folding generates eight band touching points. Black solid (dotted) circles indicate the band touching points between two bands having the same (opposite) P_x eigenvalues.

Once we introduce a density-wave order parameter with the ordering wave vector $\mathbf{Q}=(\pi,0)$, the unit cell doubles along the x direction, which leads to the Brillouin-zone folding in momentum space. Thus within the reduced Brillouin zone (RBZ), we have four bands dispersing along the k_y axis. Note that the zone folding generates eight band touching points, which are indicated by circles in Fig. 2(c). Here the band touching point between two bands with the same (opposite) P_x eigenvalues is encircled by a solid (dotted) circle.

The degeneracy between two states, $|\psi_1(\mathbf{k})\rangle$ and $|\psi_2(\mathbf{k}+\mathbf{Q})\rangle$, touching at the momentum $\mathbf{k}$ after the Brillouin-zone folding, is lifted when the matrix element of the density-wave order parameter $\hat{D}_i$ between these two states is finite, that is, $\langle\psi_1(\mathbf{k})|\hat{D}_i|\psi_2(\mathbf{k}+\mathbf{Q})\rangle\neq 0$. Therefore if the order parameter $\hat{D}_i$ (or $\hat{M}_i$) is P_x even, the degeneracy is lifted when the two degenerate bands have the same P_x eigenvalues. However, the nodal point remains gapless if the two degenerate bands have the opposite P_x eigenvalues.

On the other hand, if the density-wave order parameter $\hat{D}_i$ (or $\hat{M}_i$) is P_x odd, the full Hamiltonian is not invariant under P_x anymore. However, even in this case $\langle\psi_{1,s_1}(\mathbf{k})|\hat{D}_i|\psi_{2,s_2}(\mathbf{k}+\mathbf{Q})\rangle=0$ in the weak-coupling limit, if $s_1=s_2$, where s refers to P_x eigenvalues. Namely, the matrix element of D_i, which is odd under P_x, vanishes when the two degenerate eigenstates have the same P_x eigenvalues. To understand this point clearly, let us define the eigenvector $|\phi^{(0)}_{n,s}(\mathbf{k})\rangle$ of the hopping Hamiltonian H_0 with the even $(s=+)$ or odd $(s=-)P_x$ eigenvalues. Here n is a band index. Now we turn on a small density-wave order parameter $\hat{D}_i$ which is odd under P_x. Since the P_x eigenvalue is not a good quantum number, $|\phi^{(0)}_{n,s}(\mathbf{k})\rangle$ can be contaminated by the states with the opposite P_x eigenvalue $|\phi^{(0)}_{m,\bar{s}}(\mathbf{k}+\mathbf{Q})\rangle$, leading to

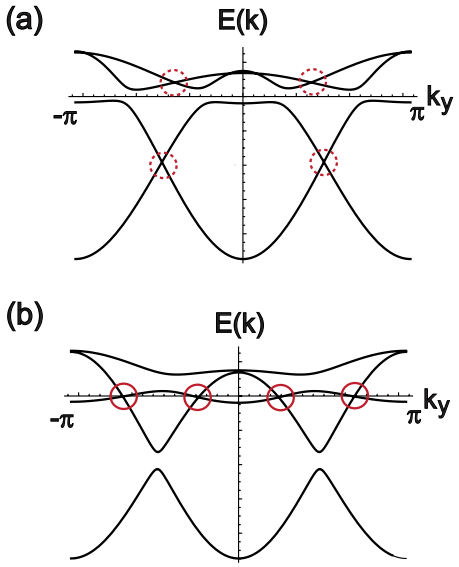

FIG. 3. (Color online) The band structures of the $\mathbf{Q}=(\pi,0)$ density-wave ground states along the k_y axis. (a) For P_x even density-wave states. (b) For P_x odd density-wave states.

$$|\phi^{(0)}_{n,s}(\mathbf{k})\rangle \xrightarrow{\hat{D}_i} |\psi_{n,s}(\mathbf{k})\rangle = |\phi_s(\mathbf{k})\rangle + |\phi_{\bar{s}}(\mathbf{k}+\mathbf{Q})\rangle,$$

where $|\phi_s(\mathbf{k})\rangle=\Sigma_n c_n|\phi^{(0)}_{n,s}(\mathbf{k})\rangle$ is a linear combination of the states with the P_x eigenvalue of s, while $|\phi_{\bar{s}}(\mathbf{k}+\mathbf{Q})\rangle=\Sigma_n c'_n|\phi^{(0)}_{n,\bar{s}}(\mathbf{k}+\mathbf{Q})\rangle$ is a linear combination of the states with the opposite P_x eigenvalue of $\bar{s}$. Notice that $|\phi_s(\mathbf{k})\rangle$ and $|\phi_{\bar{s}}(\mathbf{k}+\mathbf{Q})\rangle$ have a momentum difference given by the ordering wave vector $\mathbf{Q}$ carried by the density-wave order parameter $\hat{D}_i$. Because of the fact that the two components of the wave function with the opposite P_x eigenvalues have the momentum difference given by $\mathbf{Q}$, it is straight forward to show that $\langle\psi_{1,s_1}(\mathbf{k})|\hat{D}_i|\psi_{2,s_2}(\mathbf{k}+\mathbf{Q})\rangle=0$ if $s_1=s_2$.

Therefore the nodal point remains gapless if the order parameter $\hat{D}_i$ is P_x even (P_x odd) while the two generated bands have the opposite (same) P_x eigenvalues. It means that four nodal points among the eight band touching points remain gapless independent of the condition that the order parameter is even or odd under P_x reflection symmetry.

In Fig. 3 we plot the band structure of the density-wave ground states along the k_y axis. Figure 3(a) corresponds to the density-wave orders D_0, D_3, M_0, M_3, which are P_x even, while Fig. 3(b) describes the band structure for the other order parameters, D_1, D_2, M_1, M_2, which are odd under P_x symmetry. Notice that nodal points show opposite behavior for these two different classes of order parameters. Namely, when a nodal point remains gapless for one order parameter, it is gapped out for the other order parameter with the opposite P_x eigenvalue.

We can extend the same analysis to understand nodal points lying along the k_x axis. In this case we have P_y reflection symmetry mapping y to $-y$. However, compared to the previous analysis for nodal points on the k_y axis, there is one important difference in this case. Before the unit-cell doubling, we have two bands dispersing along the k_x axis. The

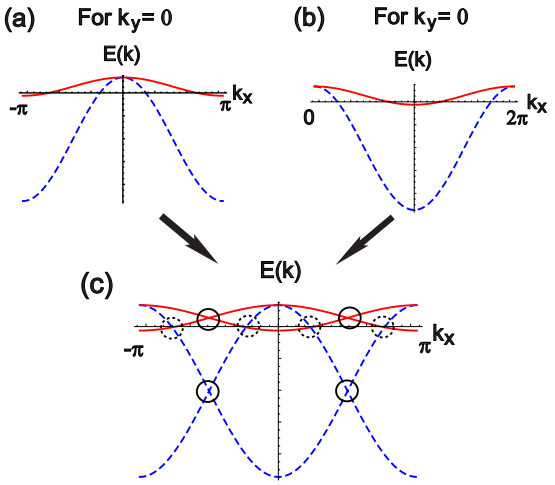

FIG. 4. (Color online) (a) Band dispersion along $k_y=0$ centered at $\mathbf{k}=(0,0)$. (b) Band dispersion along $k_y=0$ centered at $\mathbf{k}=(\pi,0)$. (c) Band structure along $k_y=0$ after the unit-cell doubling. Four bands in (a) and (b) meet and disperse together along $k_y=0$ after the Brillouin-zone folding. Here we use a red solid (blue dotted) line to indicate a band which is odd (even) under the P_y symmetry. Black solid (dotted) circles indicate the band touching points between two bands having the same (opposite) P_y eigenvalues.

Brillouin-zone folding induces overlaps of these two bands with themselves. In Fig. 4, we plot the dispersion of the two bands along the k_x axis centered at $\mathbf{k}=(0,0)$ [Fig. 4(a)] and at $\mathbf{k}=(\pi,0)$ [Fig. 4(b)]. The four bands after the zone folding displayed in Fig. 4(c) can be obtained by superposing the four bands in Figs. 4(a) and 4(b). In Fig. 4(c), we plot the band structure from $k_x=-\pi$ to $k_x=\pi$ for convenience although the first Brillouin zone is from $k_x=-\pi/2$ to $k_x=\pi/2$. Note that in Fig. 4(c) the location of solid and dotted circles are interchanged compared to those in Fig. 2(c). Because of this difference, the location of Dirac nodes along the k_x and k_y axes also show the opposite behaviors.

B. Dirac nodes from quadratic band crossing

The band structure of the two-band hopping Hamiltonian H_0 in Eq. (1) supports two quadratic band crossing points at $\mathbf{k}=(0,0)$ and $\mathbf{k}=(\pi,\pi)$.[12,22] Splitting of these quadratic band crossing points generates additional Dirac points, which contribute additional Chern numbers for various insulating phases.

Expanding the Hamiltonian $H(\mathbf{k})$ in Eq. (2) near $\mathbf{k}=(0,0)$, we obtain the following low-energy effective Hamiltonian:

$$\mathrm{H}_{\mathrm{eff}} = \int d^2k \psi^\dagger(\mathbf{k}) H_{\mathrm{quad}}(\mathbf{k}) \psi(\mathbf{k}), \tag{8}$$

in which

$$H_{\mathrm{quad}}(\mathbf{k}) = \alpha(k_x^2 + k_y^2)\hat{\tau}_0 + \beta k_x k_y \hat{\tau}_1 + \gamma(k_x^2 - k_y^2)\hat{\tau}_3, \tag{9}$$

where $\alpha=(t_1+t_2+4t_3)/2$, $\beta=-4t_4$, and $\gamma=(t_1-t_2)/2$. The nontrivial topological property of the quadratic band crossing point is reflected in the winding number N_{w}, which is defined as[19]

$$N_{\mathrm{w}} \equiv \frac{1}{\pi i}\oint_{\mathbf{C}} d\mathbf{k} \cdot \langle \psi^\dagger(\mathbf{k}) | \nabla_{\mathbf{k}} | \psi(\mathbf{k}) \rangle, \tag{10}$$

where $|\psi(\mathbf{k})\rangle$ is a Bloch wave function corresponding to one of the bands involved in the band touching and $\mathbf{C}$ is a closed loop in the momentum space encircling the band crossing point. A quadratic band crossing point contributes $N_W=\pm 2$, which is twice larger than the winding number around a Dirac point.[18–20,23]

Adding a generic perturbation given by $V=\Sigma_{i=1}^3 m_i \hat{\tau}_i$, the degeneracy at the quadratic band crossing point can be lifted. An m_2 term breaks time-reversal symmetry and the degeneracy is lifted by opening a gap. On the other hand, m_1 and m_3 terms that break fourfold rotational symmetry, split the quadratic band touching point into two Dirac points.[18–20]

Now we consider the effect of the $\mathbf{Q}=(\pi,0)$ density-wave orderings on the degeneracy lifting at quadratic band crossing points. Since the density-wave order parameters carry the momentum $\mathbf{Q}=(\pi,0)$, they cannot couple to the degenerate states at $\mathbf{k}=(0,0)$ [or $\mathbf{k}=(\pi,\pi)$] at first order. The lowest-order contribution to degeneracy lifting at quadratic band touching points starts from second-order processes. We first consider charge-density-wave order parameters given by

$$H_{\mathrm{CDW}} = \sum_{\mathbf{k},\sigma} \psi^\dagger_{\mathbf{k},\sigma} \hat{D} \psi_{\mathbf{k}+\mathbf{Q},\sigma}, \tag{11}$$

where $\hat{D}=\Sigma_{i=0}^3 D_i \hat{\tau}_i$. Treating the above H_{CDW} as a perturbation, standard second-order perturbation theory gives rise to the following effective Hamiltonian near the quadratic band touching point at $\mathbf{k}=(0,0)$:

$$H^{\mathrm{eff}}_{\mathrm{quad}} = H_{\mathrm{quad}}(\mathbf{k}) + H_{\mathrm{mass}}, = H_{\mathrm{quad}}(\mathbf{k}) + \sum_{i=0}^{3} m_\Gamma^{(i)} \hat{\tau}_i, \tag{12}$$

in which

$$\begin{aligned}
m_\Gamma^{(0)} &= \lambda\{(D_1^2 + D_2^2)(t_1 + t_2 + 4t_3) + (D_0 + D_3)^2(t_2 + 2t_3) \\
&\quad + (D_0 - D_3)^2(t_1 + 2t_3)\}, \\
m_\Gamma^{(1)} &= 2\lambda D_1\{D_3(-t_1 + t_2) + D_0(t_1 + t_2 + 4t_3)\}, \\
m_\Gamma^{(2)} &= 2\lambda D_2\{D_3(-t_1 + t_2) + D_0(t_1 + t_2 + 4t_3)\}, \\
m_\Gamma^{(3)} &= \lambda\{(D_1^2 + D_2^2)(t_1 - t_2) + (D_0 + D_3)^2(t_2 + 2t_3) \\
&\quad - (D_0 - D_3)^2(t_1 + 2t_3)\},
\end{aligned} \tag{13}$$

where $\lambda=-1/\{8(t_1+2t_3)(t_2+2t_3)\}$. Note that as long as only one of the order parameters has finite magnitude while all the other order parameters are zero, $m_\Gamma^{(1)}=m_\Gamma^{(2)}=0$. In other words, if $D_n \neq 0$ for a given n while all the other $D_{i\neq n}=0$, the quadratic band crossing point always splits into two Dirac points along the main axes.

Combining the contributions both from the Brillouin-zone folding and from the splitting of quadratic band crossing points, we show the distribution of Dirac points for a D_3 (or M_3) density-wave ground state in Fig. 5. There are four bands within the reduced Brillouin zone as shown in Fig. 5(a). We assign a band index i such that the energy eigen-

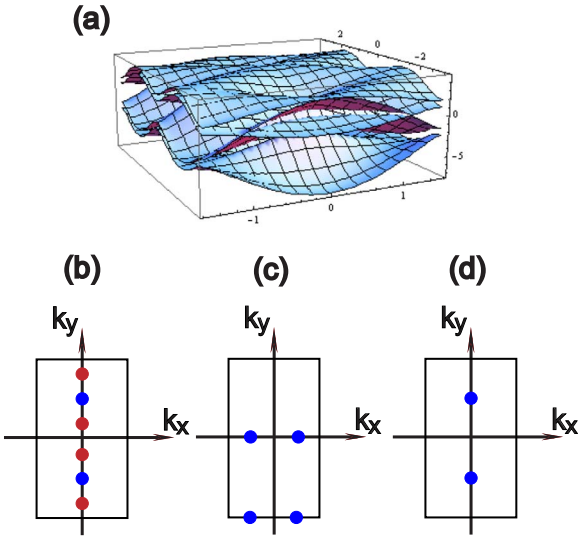

FIG. 5. (Color online) Distribution of Dirac points for the D_3 (or M_3) density-wave state. (a) Four bands within the reduced Brillouin zone. The energy eigenvalue $E_i(\mathbf{k})$ for a band i satisfies $E_1(\mathbf{k}) \geq E_2(\mathbf{k}) \geq E_3(\mathbf{k}) \geq E_4(\mathbf{k})$. (b) Dirac points between the bands 1 and 2, (c) between bands 2 and 3, and (d) between bands 3 and 4. Blue (red) dots indicates Dirac points coming from the Brillouin-zone folding (splitting quadratic band touching points).

value $E_i(\mathbf{k})$ of the band i satisfies $E_1(\mathbf{k}) \geq E_2(\mathbf{k}) \geq E_3(\mathbf{k}) \geq E_4(\mathbf{k})$. The location of Dirac points between the upper two bands (bands 1 and 2) are indicated in Fig. 5(b). Similarly, the Dirac points between the middle (bottom) two bands are described in Fig. 5(c) [Fig. 5(d)]. Notice that there are many Dirac touching points between the bands. Blue dots indicate the nodal points coming from the Brillouin-zone folding induced by the $\mathbf{Q}=(\pi,0)$ density-wave states. On the other hand, red dots result from the splitting of quadratic band touching points. Two quadratic band touching points generate four Dirac points lying on the y axis. With the understanding of the origin and locations of Dirac points, below we now discuss how to achieve TDW insulators.

IV. TOPOLOGICAL PROPERTIES OF THE GAPPED DENSITY WAVE PHASES

A single density-wave order parameter induces a metallic phase with many Dirac points. The locations of Dirac points are determined by the transformation properties of the order parameters under the reflection symmetries P_x and P_y. Therefore to get an insulating phase, two coexisting density-wave states, in which one is even and the other is odd under the P_x and P_y symmetries, are required. In addition, according to the order-parameter symmetries summarized in Table I, if time-reversal invariance is imposed, there are only four different ways of choosing a pair of density-wave order parameters, which give rise to a gapped phase. The four pairs of time-reversal invariant density-wave order parameters with the opposite transformation properties under the reflections P_x and P_y, are given by (D_3,D_1), (D_3,M_2), (D_0,D_1), and (D_0,M_2).

Since the z component of the spin S_z is conserved, the Chern number $N_{C,\sigma}^{(n)}$ is well defined for each band in a fully gapped phase.[24–26] Here $N_{C,\uparrow}^{(n)}(N_{C,\downarrow}^{(n)})$ is the Chern number of the nth spin-up (spin-down) band. For every pair of the density-wave order parameters generating a fully gapped phase, the four bands within the reduced Brillouin zone are well-separated from each other with a finite gap between any pairs of the bands. Each band is distinguished by the index n ranging from 1 to 4 as the energy decreases. The Chern number $N_{C,\sigma}^{(n)}$ of the nth band with the spin σ is defined as

$$N_{C,\sigma}^{(n)} = \frac{1}{2\pi}\int_{\mathrm{RBZ}} d^2k F_\sigma^{(n)}(\mathbf{k}), \tag{14}$$

where the momentum space Berry curvature $F_\sigma^{(n)}(\mathbf{k})$ for the nth band with the spin σ is defined as $F_\sigma^{(n)}(\mathbf{k}) \equiv \partial_{k_x} A_{y,\sigma}^{(n)}(\mathbf{k}) - \partial_{k_y} A_{x,\sigma}^{(n)}(\mathbf{k})$ in which the Berry potential $A_{\mu,\sigma}^{(n)}(\mathbf{k})$ is given by $A_{\mu,\sigma}^{(n)}(\mathbf{k}) = -i\langle \Phi_\sigma^{(n)}(\mathbf{k}) | \partial_{k_\mu} | \Phi_\sigma^{(n)}(\mathbf{k}) \rangle$.[27,28] Here the Bloch wave function $|\Phi_\sigma^{(n)}(\mathbf{k})\rangle$ is defined within the RBZ.

To facilitate numerical computation of Chern numbers, we use the following relation:

$$[J_\mu(\mathbf{k})]_{nm} \equiv \langle \Phi^{(n)}(\mathbf{k}) | \hat{J}_\mu | \Phi^{(m)}(\mathbf{k}) \rangle = [E_m(\mathbf{k}) - E_n(\mathbf{k})] \langle \Phi^{(n)}(\mathbf{k}) | \partial_{k_\mu} | \Phi^{(m)}(\mathbf{k}) \rangle, \tag{15}$$

where the current operator $\hat{J}_\mu$ is defined as $\hat{J}_\mu \equiv \partial_{k_\mu} H$ whose analytic expression can be easily obtained for any given mean field Hamiltonian H. With the current operator $\hat{J}_\mu$, the Berry curvature can be written as[29]

$$F_\sigma^{(n)}(\mathbf{k}) = -2\sum_{m\neq n} \frac{\mathrm{Im}\{[J_x(\mathbf{k})]_{mn}[J_y(\mathbf{k})]_{nm}\}}{[E_n(\mathbf{k}) - E_m(\mathbf{k})]^2}. \tag{16}$$

Explicit numerical computation of the Chern numbers using Eq. (16) shows that every band of the insulating density-wave phase with finite D_3 and M_2 has a nonzero Chern number as shown in Table II. On the other hand, every band has zero Chern number for the other three gapped phases defined with a pair of nonzero order parameters given by (D_3,D_1), (D_0,D_1), and (D_0,M_2).

TABLE II. The Chern number of each band for the gapped density-wave ground state with finite D_3 and M_2.

	$N_{C,\uparrow}$	$N_{C,\downarrow}$
Band 1	+1	−1
Band 2	−3	+3
Band 3	+3	−3
Band 4	−1	+1

A. Topological properties of the topological density-wave ground state with finite D_3 and M_2

Nontrivial topological properties of the fully gapped density-wave phase with nonzero D_3 and M_2 can be understood in the following way. We first consider the charge density-wave state with the finite D_3 order parameter. The D_3 density-wave phase supports many Dirac points whose distribution is described in Fig. 5. Now we turn on a small M_2

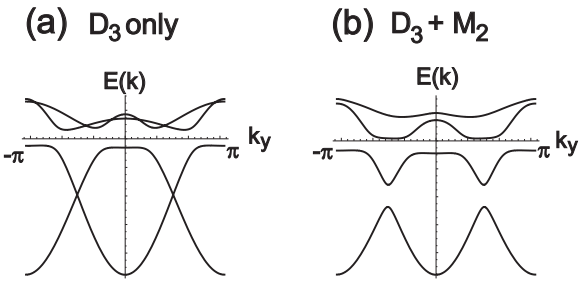

FIG. 6. (a) Band structure of the D_3 nodal density-wave state along the k_y axis. (b) Band structure of the gapped density-wave phase with finite D_3 and M_2.

which induces gap opening at each nodal point, leading to the fully gapped insulating phase, which is described in Fig. 6. The degeneracy lifting at each nodal point can be understood as a result of the mass perturbation, induced by the finite M_2, to the gapless Dirac particles. The nonzero Chern number of each band is obtained by adding up the Chern number contributions of the massive Dirac particles derived from the corresponding band.

We first focus on the two Dirac nodes lying along the k_y axis between bands 3 and 4 shown in Fig. 5(d). The effective Dirac Hamiltonian can be obtained by linearizing the Hamiltonian near the two nodal points sitting at the momentum $\mathbf{k}=\mathbf{k}_+$ and $\mathbf{k}_-$. To simplify the computational procedures, the hopping parameters t_i are slightly shifted from the initial values given in Sec. II A to $t_1=-t_2=t_3=t_4=-1.0$. This small parameter change does not affect the topological properties of the gapped phase but shifts the nodal points to $\mathbf{k}_\pm=(0,\pm\frac{\pi}{2})$ making analytical analysis simpler. The effective Hamiltonian describing the low-energy fermions near these two nodal points is given by

$$H_{\text{eff}}^{\text{Dirac}}=\sum_{\mu=\pm}\int d^2q\Psi_{\mu,\sigma}^{\dagger}(\mathbf{q})H_{\mu,\sigma}^{\text{Dirac}}(\mathbf{q})\Psi_{\mu,\sigma}(\mathbf{q}), \tag{17}$$

where

$$H_{\mu,\sigma}^{\text{Dirac}}(\mathbf{q})=-\mu\left\{\left(2+\frac{8}{\sqrt{4+D_3^2}}\right)q_y\hat{\tau}_3+\frac{4|D_3|}{\sqrt{4+D_3^2}}q_x\hat{\tau}_1\right\}. \tag{18}$$

Here the momentum $\mathbf{q}$ of the Hamiltonian $H_{\mu,\sigma}^{\text{Dirac}}(\mathbf{q})$ is measured with respect to the degeneracy point at $\mathbf{k}=\mathbf{k}_\mu(\mu=+,-)$. The two-component fermion field $\Psi_{\mu,\sigma}(\mathbf{q})$ is given by

$$\Psi_{\mu,\sigma}(\mathbf{q})=\begin{pmatrix}\alpha_1 d_{yz,\sigma}(\mathbf{k}_\mu+\mathbf{q})+\alpha_2 d_{yz,\sigma}(\mathbf{k}_\mu+\mathbf{Q}+\mathbf{q})\\ \beta_1 d_{xz,\sigma}(\mathbf{k}_\mu+\mathbf{q})+\beta_2 d_{xz,\sigma}(\mathbf{k}_\mu+\mathbf{Q}+\mathbf{q})\end{pmatrix}, \tag{19}$$

where the constant coefficients α_i and β_i satisfy $\alpha_1^2+\alpha_2^2=\beta_1^2+\beta_2^2=1$. Explicitly, α_i and $\beta_i(i=1,2)$ are given by

$$\alpha_1=(2+\sqrt{4+D_3^2})/\sqrt{8+2D_3^2+4\sqrt{4+D_3^2}},$$

$$\alpha_2=D_3/\sqrt{8+2D_3^2+4\sqrt{4+D_3^2}},$$

$$\beta_1=(2-\sqrt{4+D_3^2})/\sqrt{8+2D_3^2-4\sqrt{4+D_3^2}},$$

$$\beta_2=D_3/\sqrt{8+2D_3^2-4\sqrt{4+D_3^2}}.$$

Notice that the first (second) component of $\Psi_{\mu,\sigma}(\mathbf{q})$ is derived entirely from the $d_{yz}(d_{xz})$ orbital.

Now we include the M_2 spin-density-wave order parameter which generates a mass term in the low-energy limit given by

$$H_{M_2}^{\text{mass}}=\sum_{\mu=\pm}\int d^2q\Psi_{\mu,\sigma}^{\dagger}(\mathbf{q})\left\{-\frac{2|D_3|M_2\sigma}{D_3\sqrt{4+D_3^2}}\hat{\tau}_2\right\}\Psi_{\mu,\sigma}(\mathbf{q}). \tag{20}$$

For the given spin σ, the mass term has the same magnitude and sign at the two Dirac points. At each Dirac point, this mass term opens a gap and contributes to the Chern number $N_{C,\sigma}=+\frac{M_2\sigma}{2|M_2|}$ for the upper band (band 3) and $N_{C,\sigma}=-\frac{M_2\sigma}{2|M_2|}$ for the lower band (band 4).[8,23,30,31] Adding the Chern number contributions from the two Dirac points, the total Chern number of the band 4 with the spin σ is given by $N_{C,\sigma}^{(4)}=-\text{sgn}(M_2)\sigma$, which is consistent with the result obtained from the integration of the Berry curvature over the reduced Brillouin zone using Eq. (14). (See Table II.) In the case of the band 3, the Chern number is determined after including the additional contributions from the nodal points between bands 2 and 3.

Similarly, the trivial topological property of the gapped phase with finite D_3 and D_1 can also be understood by applying the same analysis. For the D_3 nodal density-wave state, the small D_1 charge-density-wave order parameter generates mass perturbations to Dirac particles, which can be described by the following Hamiltonian:

$$H_{D_1}^{\text{mass}}=\sum_{\mu=\pm}\int d^2q\Psi_{\mu,\sigma}^{\dagger}(\mathbf{q})\left\{\frac{2|D_3|D_1}{D_3\sqrt{4+D_3^2}}\hat{\tau}_1\right\}\Psi_{\mu,\sigma}(\mathbf{q}). \tag{21}$$

Notice that this term just induces the shifting of the nodal points away from the k_y axis. Once a Dirac point moves away from the reflection symmetry axis, the degeneracy at the band touching point is no longer protected by the symmetry and a gap opens because the density-wave order parameters support finite matrix elements between the two bands touching at the nodal point. Since the D_1 charge-density-wave order parameter does not generate a mass term to the Dirac Hamiltonian, it has no contribution to the Chern number leading to the zero Chern numbers of all bands.

We apply a similar analysis to every Dirac point derived from the Brillouin-zone folding for all pairs of density-wave order parameters generating fully gapped phases. In all cases, it is confirmed that the Chern number of each band obtained by summing up the Chern number contributions from the Dirac points is identical to the result obtained by the integration of the Berry curvature in the momentum space.

In addition, the coexisting D_3 and M_2 density-wave order parameters also lift the degeneracies of the two quadratic band touching points at $\mathbf{k}=(0,0)$ and $(0,\pi)$ leading to a fully gapped band structure. In contrast to the case of Dirac points, the Chern number obtained by lifting a quadratic band degeneracy is two times larger than the contribution from a

TABLE III. Spin Chern numbers and topological Z_2 invariants for the gapped density-wave ground state with finite D_3 and M_2.

Band filling	Spin Chern number (C_S)	Z_2 invariant (ν)
3/4	−2	1
1/2	+4	0
1/4	−2	1

single Dirac point. However, since the two quadratic band crossing points lead to the Chern number contributions with the opposite signs, the net effect of the two quadratic band touching points vanishes.

Since the four bands are well separated from each other for the topological density-wave phase with $D_3 \neq 0$ and $M_2 \neq 0$, if the magnitude of the order parameter M_2 is large enough, an insulating ground state is obtained whenever the Fermi level lies in the gap between two neighboring bands. Therefore there are three different insulating phases, in principle, whenever the Fermi level lies between the band n and $n+1$ $(n=1,2,3)$ corresponding to the band filling factor $N_{\text{filling}}=(4-n)/4$. The topological property of the insulating phase can be explicitly characterized by computing topological invariants. We first consider the spin Chern number C_S which is defined in the following way:

$$C_S = \sum_{n \in occ} \{N_{C,\uparrow}^{(n)} - N_{C,\downarrow}^{(n)}\}, \tag{22}$$

where the summation includes all the occupied bands. When the S_z is conserved, the spin Chern number C_S is quantized and characterizes the two-dimensional topological insulators.[24] In Table III we show the spin Chern numbers for the insulating phases. It is interesting that the spin Chern numbers are nonzero for all cases. Therefore as long as the z component of the spin is conserved, we can obtain the topological insulator with finite spin Hall conductivity for every quarter filling. However, in the presence of spin nonconserving perturbations and disorders, the spin Chern number is not well defined and conserved only modulo 4.[26,32] In other words, when the S_z is not conserved, the half-filled system is equivalent to the phase with zero-spin Chern number, which is nothing but a topologically trivial band insulator. However, it is important to notice that even in this case the system remains as a topological insulator with nonzero Z_2 topological invariant for 1/4 and 3/4 fillings.

We also compute the Z_2 topological invariant ν shown in Table III, which can be used to distinguish topological insulators $(\nu=1)$ from trivial band insulators $(\nu=0)$ for generic time-reversal invariant systems. Since the system has the inversion symmetry, the Z_2 invariant can be obtained from the parity eigenvalues $\xi_m(\Gamma_l)$ of the occupied bands with the band indices m at the time-reversal invariant momenta $\mathbf{\Gamma_l}$.[33] Using the reciprocal lattice vectors $\mathbf{G}_i$ $(i=1,2)$, the four time reversal invariant momenta can be written as $\mathbf{\Gamma_{l=n_1n_2}}=(n_1\mathbf{G}_1+n_2\mathbf{G}_2)/2$, with $n_{1,2}=0,1$. The inversion parities of the bands at the time reversal invariant momenta are shown in Table IV. Explicitly the Z_2 topological invariant ν is given by

TABLE IV. Inversion parities of the bands in the topological density-wave phase. Here +(−) means the even (odd) parity of the band at a time-reversal invariant momentum within the reduced Brillouin zone.

	(0,0)	$(0,\pi)$	$(\pi/2,0)$	$(\pi/2,\pi)$
Band 1	−	−	+	−
Band 2	−	−	−	+
Band 3	−	−	−	+
Band 4	−	−	+	−

$$(-1)^{\nu} = \prod_{n_i=0,1} \prod_{m} \xi_m(\mathbf{\Gamma_{n_1n_2}}), \tag{23}$$

where the parity eigenvalues of the occupied bands at the four time-reversal invariant momenta are multiplied. Because of time reversal symmetry, each band is doubly degenerate at the time reversal invariant momentum and every Kramers doublet shares the same inversion parity. The Z_2 topological invariant counts the parity of one state for each Kramers pair.[33]

As shown in Table III, the Z_2 topological insulators exist when the band filling is one-quarter or three-quarter. However, the 3/4 filled case requires unreasonably large M_2 to achieve an insulating phase. This is because, as shown in Fig. 6, the overall structures of the bands 1 and 2 are in parallel. To open a full gap between the upper two bands (bands 1 and 2), the magnitude of the M_2 density-wave order parameter should be as large as their bandwidth. Therefore the quarter-filled system is the most favorable for the realization of the Z_2 topological insulator.

To support further the nontrivial topological properties of the topological density-wave phase with $D_3 \neq 0$ and $M_2 \neq 0$, we compute the edge state spectrum by considering the Hamiltonian on a strip geometry, which is infinite in the x direction but finite in the y direction with open boundaries at

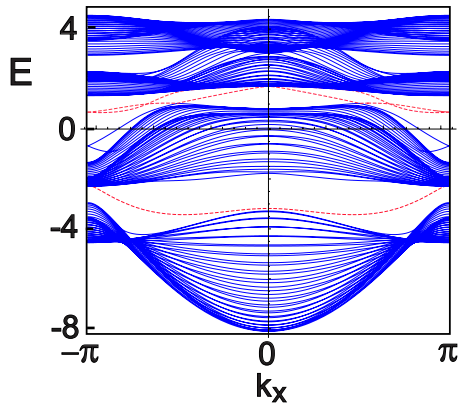

FIG. 7. (Color online) Energy spectrum for the topological density-wave ground state with $D_3=0.85$ and $M_2=0.75$ in a strip geometry with the hopping parameters given by $t_1=-1.0$, $t_2=1.3$, and $t_3=t_4=-0.85$. Here we use open boundary conditions with $N_y=40$ sites along the y direction. The red dotted lines stand for edge states, all of which are doubly degenerate. For 1/2 filling, the number of edge states is twice larger than that for ¼ filling.

$y=1$ and $y=N_y$. Here N_y indicates the number of lattice sites in the y direction. The energy spectrum of the system with $N_y=40$ is described in Fig. 7, which shows the existence of robust gapless edge states traversing between the lower two bands (bands 3 and 4) and the middle two bands (bands 2 and 3). The upper two bands (bands 1 and 2) are not well separated for $D_3=0.85$ and $M_2=0.75$, which are used to obtain the energy spectrum. Each edge state represented by a red dotted line is doubly degenerate, one with spin up and the other with spin down. For the 1/4 filling with the chemical potential lying in the gap between the bands 3 and 4, there are two gapless edges states on each boundary propagating in the opposite directions with the opposite spin quantum numbers. On the other hand, for the 1/2 filling, there are four gapless edge states on each boundary consistent with the fact that the spin Chern number $C_S=4$ whose magnitude is twice larger than that for the 1/4 filling with $C_S=-2$. Therefore, for the collinear spin ordering with $M_2\neq 0$, which conserves S_z, there are robust gapless edge states for both the quarter-filled and half-filled systems.

B. Comparison to the honeycomb lattice

It is interesting that a simple on-site density-wave order parameter can generate insulating phases with nontrivial topological properties. This result can be contrasted with the topological insulator on the honeycomb lattice where complex second neighbor hopping processes are required to obtain a topological insulator while the simple on-site staggered chemical potential gives rise to a trivial band insulator.[4,5,10] It is the distinct topological properties of the Dirac particles in the D_3 nodal density-wave phase in the d-orbital system which make it possible to realize the topological insulator by introducing a simple on-site order parameter M_2.

In this subsection, we discuss the topological property of the Dirac particles in the D_3 nodal density-wave state in detail and compare it with the topological property of the Dirac particles on the honeycomb lattice. In the forthcoming discussion we neglect the spin degrees of freedom and focus on the condition under which the insulating phase possesses a finite Chern number, which is nothing but a Chern insulator. Once we find the condition to obtain a Chern insulator, the time-reversal invariant topological insulator can be realized by superposing two Chern insulators with spin-up and spin-down particles, respectively.

The topological property of the Dirac particles in the D_3 nodal density-wave state can be understood in the following way. The low-energy Hamiltonian $H_{\pm}^{\mathrm{Dirac}}$ in Eq. (18) for the Dirac particles near the momentum $\mathbf{k}=\mathbf{k}_{\pm}$, where the band touching points between the bands 3 and 4 locate, can be written as

$$H_{\pm}^{\mathrm{Dirac}}(\mathbf{q}) = h_{\pm,x}(\mathbf{q})\hat{\tau}_1 + h_{\pm,y}(\mathbf{q})\hat{\tau}_3. \tag{24}$$

Since $\sqrt{h_{\pm,x}^2(\mathbf{q})+h_{\pm,y}^2(\mathbf{q})}$ is nonzero away from the degeneracy point, a two component vector $\vec{d}_{\pm}(\mathbf{q})$ with unit length can be defined as

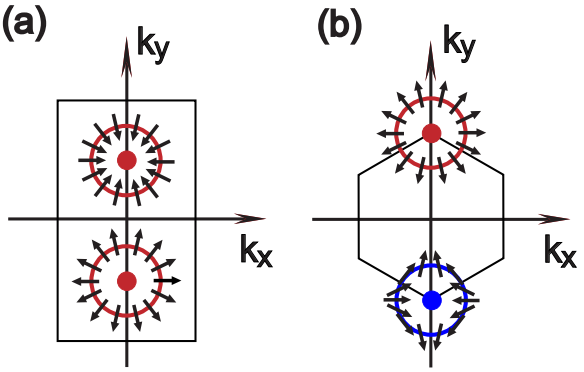

FIG. 8. (Color online) The winding directions of the $\vec{d}(\mathbf{q})$ vector around the Dirac point. Black arrows describe the two component $\vec{d}=(d_x,d_y)$ vector in Eq. (25) along the circular path around the Dirac point at the center. (a) For the two Dirac points between the band 3 and band 4 in the nodal density-wave state with the finite D_3. The $\vec{d}$ vector has the same winding direction around the two Dirac points. (b) For the two Dirac points on the graphene system. The $\vec{d}$ vector has the opposite winding directions around the two Dirac points.

$$\vec{d}_{\pm}(\mathbf{q}) = [d_{\pm,x}(\mathbf{q}), d_{\pm,y}(\mathbf{q})] \equiv \frac{[h_{\pm,x}(\mathbf{q}), h_{\pm,y}(\mathbf{q})]}{\sqrt{h_{\pm,x}^2(\mathbf{q})+h_{\pm,y}^2(\mathbf{q})}}. \tag{25}$$

Along the circle C_R satisfying $q_x^2+q_y^2=R^2\neq 0$ with the degeneracy point at the center, the 2D unit vector $\vec{d}_{\pm}(\mathbf{q})$ defines a map from the circle C_R to the unit circle S^1. Since the fundamental group $\pi_1(S^1)=Z$, the 2D unit vector $\vec{d}_{\pm}(\mathbf{q})$ has an integer-valued topological invariant, which is nothing but the winding number N_{w} defined in Eq. (10). In terms of the 2D unit vector $\vec{d}_{\pm}(\mathbf{q})$, the winding number N_{w} can be rewritten as

$$N_{\mathrm{w}} = \frac{1}{2\pi}\oint_{C_R} d\theta \hat{z}\cdot\left(\vec{d}\times\frac{d\vec{d}}{d\theta}\right), \tag{26}$$

where the loop integral is defined along the circle where the momentum $\mathbf{q}=Re^{i\theta}$.[34]

In Fig. 8(a) we describe the directions of the two-component $\vec{d}$ vector along the circular path around the Dirac points for the D_3 nodal density-wave state. Notice that the $\vec{d}$ vector has the same winding direction with the winding number of $N_{\mathrm{w}}=1$ around the two Dirac points. The two Dirac points share the same winding number because of the constraint imposed by lattice symmetries. Since the first (second) component of the two-component Dirac field $\Psi_{\mu}(q)$ is given by the $d_{yz}(d_{xz})$ orbital state, $\Psi_{\mu}(q)$ transforms to $-\Psi_{\bar{\mu}}(-q)$ under inversion due to the odd parity of d_{xz} and d_{yz} orbitals. Here $\bar{\mu}$ has the opposite sign of μ. This imposes the following constraint on the pair of Dirac Hamiltonians related by inversion symmetry,

$$H_{+}^{\mathrm{Dirac}}(\mathbf{q}) = H_{-}^{\mathrm{Dirac}}(-\mathbf{q}). \tag{27}$$

This constraint guarantees the same winding numbers for the two Dirac Hamiltonians H_{+}^{Dirac} and H_{-}^{Dirac}. It is important to notice that every pair of Dirac Hamiltonians related by in-

version symmetry satisfies the same constraint for nodal density-wave phases.

The fact that a pair of Dirac Hamiltonians related by inversion symmetry have the same winding numbers is the distinct topological property of the Dirac particles in the nodal density-wave states, distinguishable from the topological properties of the Dirac particles in the honeycomb lattice. In this system, the two Dirac points at the corners of the first Brillouin zone have the opposite winding directions, which is described in Fig. 8(b). Since the inversion symmetry interchanges the two sublattices of the honeycomb lattice, each of which comprises one component of the Dirac fermion field $\Psi_\mu(\mathbf{q})$, the Dirac fermion field $\Psi_\mu(\mathbf{q})$ transforms, for example, to $\hat{\tau}_x\Psi_{\bar{\mu}}(-\mathbf{q})$ under inversion symmetry. This imposes the following constraint on the two Dirac Hamiltonians related by inversion symmetry:

$$H_+^{\mathrm{Dirac}}(\mathbf{q}) = \hat{\tau}_x H_-^{\mathrm{Dirac}}(-\mathbf{q})\hat{\tau}_x. \tag{28}$$

The additional Pauli matrix reverses the winding direction of one of the $\vec{d}$ vectors, leading to two Dirac Hamiltonians with opposite winding numbers. Therefore these two Dirac points can be pair annihilated when they are brought together by perturbations.[3,13]

The relative winding numbers of the pair of Dirac Hamiltonians related by inversion symmetry strongly constrain the topological properties of the insulating phases obtained by mass perturbations to the Dirac particles. The introduction of a constant mass term $H_\pm^{\mathrm{mass}}=m\hat{\tau}_2$ to the Dirac Hamiltonian in Eq. (24) gives rises to the third component $d_z(\mathbf{q})$ of the corresponding $\vec{d}$ vector.[18,24] Explicitly, for the massive Dirac Hamiltonian given by

$$H^{\mathrm{Dirac}}(\mathbf{q}) = h_x(\mathbf{q})\hat{\tau}_1 + h_y(\mathbf{q})\hat{\tau}_3 + m\hat{\tau}_2, \tag{29}$$

the three-dimensional (3D) unit vector $\vec{d}_{3\mathrm{D}}$ is defined as

$$\vec{d}_{3\mathrm{D}}(\mathbf{q}) = (d_x(\mathbf{q}),d_y(\mathbf{q}),d_z(\mathbf{q})) \equiv \frac{(h_x(\mathbf{q}),h_y(\mathbf{q}),m)}{\sqrt{h_x^2(\mathbf{q})+h_y^2(\mathbf{q})+m^2}}. \tag{30}$$

If we introduce, for instance, a positive mass term to the two Dirac Hamiltonians corresponding to the D_3 nodal density-wave phase described in Fig. 8(a), both of the $\vec{d}_{3\mathrm{D}}$ vectors, which have positive z components, move along the northern hemisphere as the momentum $\mathbf{q}$ sweeps over the two-dimensional momentum space. The net solid angles subtended by these two $\vec{d}_{3\mathrm{D}}$ vectors over the entire momentum space are the same, each of which covers 2π. At this point, it is useful to take into account the following relation between the Chern number of the valence band and the 3D unit vector $\vec{d}_{3\mathrm{D}}$ for the two band Hamiltonian in Eq. (29) (Ref. 18):

$$N_C = \int \frac{d^2k}{4\pi}\vec{d}_{3\mathrm{D}}\cdot(\partial_{k_x}\vec{d}_{3\mathrm{D}}\times\partial_{k_y}\vec{d}_{3\mathrm{D}}). \tag{31}$$

The above identity implies that the Chern number counts the number of times the 3D unit vector $\vec{d}_{3\mathrm{D}}$ winds around the unit sphere over the Brillouin-zone torus. Therefore, when a constant mass term is added to the two Dirac points connected by inversion symmetry, the Chern number $N_C=\pm 1$ if the two Dirac points have the same winding numbers, which is realized in the nodal density-wave ground state.

In contrast, the net solid angles covered by the two $\vec{d}_{3\mathrm{D}}$ vectors in the honeycomb lattice have the same magnitudes but with the opposite signs. Therefore the total solid angle covered by these two $\vec{d}_{3\mathrm{D}}$ vectors vanishes. The vanishing Chern number contributions from the two Dirac points leads to the topologically trivial insulating phase when the simple mass term in Eq. (29) is introduced. This contrasting behavior of the pair of 3D unit vectors $\vec{d}_{3\mathrm{D}}$ in these two systems results in the distinct topological properties of the insulating phases, the topological insulator in the d-orbital system and the topologically trivial band insulator in the honeycomb lattice when constant mass terms with the same signs are added to the pair of Dirac points connected by inversion symmetry. However, if we introduce mass terms with the opposite signs at the two Dirac points in graphene, a topological insulator with a finite Chern number can be obtained, which is realized by considering the complex second nearest-neighbor hopping processes on the honeycomb lattice.

V. MEAN-FIELD THEORY

Now we address the question whether the TDW insulator with finite D_3 and M_2 can be achieved in real systems. In particular, by taking into account the interactions between electrons, we investigate the conditions to realize the TDW insulator via spontaneous symmetry breaking. Previous mean field studies on the two-orbital Hubbard model with the hopping Hamiltonian H_0 in Eq. (1) show that the leading instability of the system is the uniform spin-density-wave phase (M_0-SDW), which is described by nonzero M_0. However, there exist other density-wave order parameters including imaginary charge- and spin-density-wave states, which are competing with the uniform spin-density-wave state (M_0-SDW) with small energy differences.[16,35,36] Therefore, if we include longer range interactions, which are not included in the multiorbital on-site Hubbard Hamiltonian, other competing ground states, for example, the topological density-wave (TDW) state, can replace the M_0-SDW state.

Including on-site and intersite electron-electron interactions, the full Hamiltonian is given by

$$H_{\mathrm{full}} = H_0 + H_{\mathrm{onsite}} + H_{\mathrm{intersite}}, \tag{32}$$

in which

$$\begin{aligned} H_{\mathrm{onsite}} = {} & U\sum_i \sum_{a=1,2} n_{i,a,\uparrow}n_{i,a,\downarrow} + U_2\sum_i n_{i,1}n_{i,2} \\ & + J_H\sum_i \sum_{\sigma_1,\sigma_2} d^\dagger_{i,1,\sigma_1}d^\dagger_{i,2,\sigma_2}d_{i,1,\sigma_2}d_{i,2,\sigma_1} \\ & + J_H\sum_i (d^\dagger_{i,1,\uparrow}d^\dagger_{i,1,\downarrow}d_{i,2,\downarrow}d_{i,2,\uparrow} + \mathrm{H.c.}) \end{aligned} \tag{33}$$

and

$$H_{\text{intersite}} = V_{1A}\sum_{\langle ij\rangle}\sum_{a=1,2} n_{i,a}n_{j,a} + V_{1B}\sum_{\langle ij\rangle} n_{i,1}n_{j,2} + V_{2A}\sum_{\langle\langle ij\rangle\rangle}\sum_{a=1,2} n_{i,a}n_{j,a} + V_{2B}\sum_{\langle\langle ij\rangle\rangle} n_{i,1}n_{j,2}, \quad (34)$$

where H_0 indicates the hopping Hamiltonian in Eq. (1). For the on-site interactions described by H_{onsite}, the intraorbital repulsion U, the interorbital repulsion U_2, and the Hund's coupling J_H are considered. In the $H_{\text{intersite}}$ describing the intersite Coulomb interactions, $V_{1A}(V_{1B})$ indicates the nearest-neighbor Coulomb repulsion between electrons in the same (different) kinds of orbitals. Finally, $V_{2A}(V_{2B})$ indicates the next nearest-neighbor Coulomb repulsion between electrons in the same (different) kinds of orbitals.

To investigate the existence of the TDW state with $D_3 \neq 0$ and $M_2 \neq 0$ and its competition with the uniform spin-density-wave phase (M_0-SDW), we apply a mean-field approximation to the Hamiltonian H_{full}. The resulting mean-field Hamiltonian is given by

$$H_{\text{MF}} = H_0 + N\epsilon_0 + \sum_{\mathbf{k}\in\mathbf{RBZ},\sigma}[A_{11,\sigma}\{d^\dagger_{1,\sigma}(\mathbf{k})d_{1,\sigma}(\mathbf{k}+\mathbf{Q}) + d^\dagger_{1,\sigma}(\mathbf{k}+\mathbf{Q})d_{1,\sigma}(\mathbf{k})\} + A_{22,\sigma}\{d^\dagger_{2,\sigma}(\mathbf{k})d_{2,\sigma}(\mathbf{k}+\mathbf{Q}) + d^\dagger_{2,\sigma}(\mathbf{k}+\mathbf{Q})d_{2,\sigma}(\mathbf{k})\}$$
$$+ A_{12,\sigma}\{d^\dagger_{1,\sigma}(\mathbf{k})d_{2,\sigma}(\mathbf{k}+\mathbf{Q}) + d^\dagger_{1,\sigma}(\mathbf{k}+\mathbf{Q})d_{2,\sigma}(\mathbf{k})\} + A_{21,\sigma}\{d^\dagger_{2,\sigma}(\mathbf{k})d_{1,\sigma}(\mathbf{k}+\mathbf{Q}) + d^\dagger_{2,\sigma}(\mathbf{k}+\mathbf{Q})d_{1,\sigma}(\mathbf{k})\}], \quad (35)$$

in which

$$\epsilon_0 = \frac{U}{8}(M_0^2 - D_3^2) + \frac{U_2}{8}(M_2^2 + 2D_3^2) + \frac{J_H}{8}(M_0^2 - D_3^2 - M_2^2) + \left(V_{2A} - \frac{V_{2B}}{2}\right)D_3^2 \quad (36)$$

and

$$A_{11,\sigma} = \frac{U}{4}(D_3 - \sigma M_0) - \frac{U_2}{2}D_3 - (2V_{2A} - V_{2B})D_3 + \frac{J_H}{4}(-D_3 + \sigma M_0),$$

$$A_{22,\sigma} = -\frac{U}{4}(D_3 + \sigma M_0) + \frac{U_2}{2}D_3 + (2V_{2A} - V_{2B})D_3 + \frac{J_H}{4}(D_3 + \sigma M_0),$$

$$A_{12,\sigma} = A^*_{21,\sigma} = \frac{U_2}{4}i\sigma M_2 - \frac{J_H}{4}i\sigma M_2. \quad (37)$$

Note that the nearest-neighbor Coulomb repulsions V_{1A} and V_{1B} do not contribute to the mean-field Hamiltonian because the order parameters have the ordering wave vector $\mathbf{Q} = (\pi, 0)$.

The order parameters M_0, M_2, D_3 are determined by solving the following self-consistent equations:

$$M_0 = \frac{1}{N}\sum_{\mathbf{r}=(r_x,r_y)}\sum_{\sigma=\pm}(-1)^{r_x}\sigma\langle d^\dagger_{\mathbf{r},1,\sigma}d_{\mathbf{r},1,\sigma} + d^\dagger_{\mathbf{r},2,\sigma}d_{\mathbf{r},2,\sigma}\rangle,$$

$$M_2 = \frac{1}{N}\sum_{\mathbf{r}=(r_x,r_y)}\sum_{\sigma=\pm}(-1)^{r_x}\sigma\langle id^\dagger_{\mathbf{r},1,\sigma}d_{\mathbf{r},2,\sigma} - id^\dagger_{\mathbf{r},2,\sigma}d_{\mathbf{r},1,\sigma}\rangle,$$

$$D_3 = \frac{1}{N}\sum_{\mathbf{r}=(r_x,r_y)}\sum_{\sigma=\pm}(-1)^{r_x}\langle d^\dagger_{\mathbf{r},1,\sigma}d_{\mathbf{r},1,\sigma} - d^\dagger_{\mathbf{r},2,\sigma}d_{\mathbf{r},2,\sigma}\rangle. \quad (38)$$

The chemical potential μ is also determined self-consistently to satisfy the half-filling condition.

The resulting mean field phase diagram is shown in Fig. 9. Here we choose $U=5$, $J_H=0$ and compute the ground state phase diagram as a function of the interorbital on-site repulsion U_2 and effective next-nearest-neighbor repulsion $V_{2,\text{eff}} \equiv V_{2B} - 2V_{2A}$. In the absence of the intersite interactions $V_{2,\text{eff}}=0$, the uniform spin-density-wave phase (M_0-SDW) dominates the phase diagram consistent with the previous studies. However, the interorbital on-site repulsion U_2 suppresses the uniform spin-density-wave states (M_0-SDW) which is diagonal in the orbital space, but promotes the M_2-SDW, which is off-diagonal in the orbital space, to the ground state. On the other hand, the D_3 charge-density-wave phase (D_3-CDW) is strongly affected by the next-nearest-neighbor Coulomb repulsions V_{2A} and V_{2B}. In particular, the V_{2A}, the next-nearest-neighbor repulsion between the electrons in the same kinds of orbitals, strongly favors the D_3-CDW because the staggered orbital ordering described by D_3-CDW can avoid the energy cost coming from V_{2A}. Notice that there is a finite range in the parameter space where both M_2-SDW and D_3-CDW are nonzero realizing the TDW phase.

The above mean-field phase diagram is obtained for the half-filled case where the topological property of the TDW

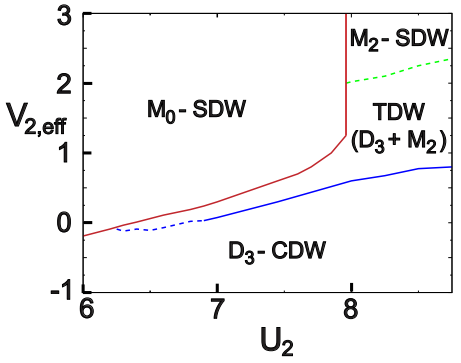

FIG. 9. (Color online) Mean-field phase diagram with the hopping parameters given by $t_1=-1.0$, $t_2=1.3$, and $t_3=t_4=-0.85$. Here we set $U=5$, $J_H=0$ and plot the ground state phase diagram varying the interorbital on-site repulsion U_2 and the effective next-nearest-neighbor repulsion $V_{2,\mathrm{eff}}=V_{2B}-2V_{2A}$. There is a finite range between D_3 charge-density-wave phase (D_3-CDW) and M_2 spin-density-wave phase (M_2-SDW) where the topological density-wave (TDW) phase becomes the ground state. Solid (dotted) lines indicate the first (second) order phase transitions.

phase is not robust against perturbations breaking S_z symmetry. On the other hand, the TDW insulator at 1/4 filling maintains its topological properties as long as time-reversal symmetry is preserved. It was shown, in the study of the single orbital extended Hubbard model, that the next-nearest-neighbor interaction (V_{2A} for our model) stabilizes a stripe pattern charge ordering with the momentum $\mathbf{Q}=(\pi,0)$.[37] This occurs at 1/4 filling when the on-site Hubbard interaction U is much stronger than the hopping amplitude t satisfying $U \gg t$ so that double occupancy is almost frozen. In our model, there are two orbitals of d_{xz} and d_{yz}. Similar to the single orbital case, we find that the next-nearest-neighbor interaction stabilizes D_3 order. Therefore, when the on-site intraorbital and interorbital interactions satisfy $U, U_2 \gg t$, the D_3-CDW ordering should be favored at 1/4 filling.

To get a TDW insulator, finite M_2 is required in addition to D_3. As shown in Sec. II B, the M_2 order parameter is equivalent to a staggered spin-orbit coupling, $\sim\Sigma_i(-1)^{i_x} S_{i,z} L_{i,z}$. One can show that when spin-orbit interaction is present, an M_2 term can be induced as long as D_3 sets in since D_3 leads to unequal density between d_{xz} and d_{yz} orbitals. Therefore, we expect that the TDW insulator can be obtained by tuning V_{2B} when $U, U_2 \gg t$ at 1/4 filling in the presence of spin-orbit coupling.

VI. TOPOLOGICAL INSULATORS IN THREE-BAND SYSTEMS

In the preceding sections, we have focused on a two-band tight-binding Hamiltonian, which consists of d_{xz} and d_{yz} orbitals. However, the main idea for realizing topological insulators using two density-wave order parameters with opposite symmetries under reflections is valid in general and applicable to more realistic multiorbital systems. Here we extend our analysis to a three-band model composed of d_{xz}, d_{yz}, and d_{xy} orbitals. In particular, we apply our idea to a more realistic model Hamiltonian relevant to the iron pnictide system, which is a representative itinerant multiband system manifesting a density-wave ground state with the ordering wave vector $\mathbf{Q}=(\pi,0)$.[35,38–41] Here we adopt the three-orbital model proposed by Daghofer *et al.*,[38] which captures the main physical properties of the Fe-pnictide systems. In momentum space, the effective three-band tight-binding Hamiltonian is given by

$$\mathrm{H}_{3\mathrm{band}} = \sum_{\mathbf{k},\sigma} \sum_{\mu,\nu} d^{\dagger}_{\mu,\sigma}(\mathbf{k}) T^{\mu\nu}(\mathbf{k}) d_{\nu,\sigma}(\mathbf{k}), \tag{39}$$

where

$$T^{11} = 2t_2 \cos k_x + 2t_1 \cos k_y + 4t_3 \cos k_x \cos k_y - \mu_c,$$

$$T^{22} = 2t_1 \cos k_x + 2t_2 \cos k_y + 4t_3 \cos k_x \cos k_y - \mu_c,$$

$$T^{33} = 2t_5(\cos k_x + \cos k_y) + 4t_6 \cos k_x \cos k_y - \mu_c + \Delta_{xy},$$

$$T^{12} = T^{21} = 4t_4 \sin k_x \sin k_y,$$

$$T^{13} = (T^{31})^* = 2it_7 \sin k_x + 4it_8 \sin k_x \cos k_y,$$

$$T^{23} = (T^{32})^* = 2it_7 \sin k_y + 4it_8 \sin k_y \cos k_x. \tag{40}$$

Here we use the unfolded Brillouin zone satisfying $-\pi < k_x, k_y \leq \pi$ as before, which corresponds to one iron atom per unit cell. In real iron pnictide materials, the unit cell contains two Fe atoms due to the buckling of the As atoms. Therefore the unit translations along the $x(T_x)$ and $y(T_y)$ directions by the nearest-neighbor Fe-Fe distance, are not the symmetries of the system. However, as pointed out in Ref. 39, the system is invariant under translation combined with the reflection P_z with respect to the xy plane, i.e., $P_z T_x$ and $P_z T_y$. Then the eigenstates can be labeled by a pseudocrystal momentum corresponding to the eigenvalues of the combined operations $P_z T_x$ and $P_z T_y$ with one iron atom per unit cell. We use this pseudocrystal momentum to label states for the momentum space representation of the Hamiltonian in Eq. (39).

In Eqs. (39) and (40), $\mu=1, 2, 3$ indicate d_{xz}, d_{yz}, and d_{xy} orbitals, respectively. Δ_{xy} represents the atomic potential of d_{xy} orbital relative to d_{xz} and d_{yz} orbitals. The chemical potential is given by μ_c. The hopping parameters are displayed in Table V, which are determined in Ref. 38. For 2/3 filling,[38] there are two hole pockets near the Γ point and two electron pockets at the X and Y points, which are consistent with the

TABLE V. Parameters for the three-band tight-binding Hamiltonian (Ref. 42).

t_1	t_2	t_3	t_4	t_5	t_6	t_7	t_8	Δ_{xy}
0.02	0.06	0.03	−0.01	0.2	0.3	−0.2	0.12	0.4

TABLE VI. Symmetry of the charge density order parameters with the momentum $(\pi,0)$. Here "+" ("−") indicates "even" ("odd") parity of order parameters under the corresponding symmetry operation. The complex off-diagonal components $D_{ij}(i\neq j)$ are decomposed as $D_{ij}=D_{ij}^R+iD_{ij}^I$.

	D_{11}	D_{22}	D_{33}	D_{12}^R	D_{12}^I	D_{13}^R	D_{13}^I	D_{23}^R	D_{23}^I
P_xP_z	+	+	+	−	−	−	−	+	+
P_yP_z	+	+	+	−	−	+	+	−	−
I	+	+	+	+	+	−	−	−	−
T	+	+	+	+	−	+	−	+	−

local-density approximation (LDA) calculations and angle-resolved photoemission spectroscopy (ARPES) measurement for LaOFeAs.

Density-wave order parameters with the momentum $\mathbf{Q}=(\pi,0)$ can be described by the following Hamiltonian:

$$\hat{H}_{\mathrm{CDW}}=\sum_{i,\sigma}\sum_{a,b=1}^{3}(-1)^{i_x}D_{ab}d_{i,a,\sigma}^{\dagger}d_{i,b,\sigma},$$

$$\hat{H}_{\mathrm{SDW}}=\sum_{i,\sigma_1\sigma_2}\sum_{a,b=1}^{3}(-1)^{i_x}M_{ab}d_{i,a,\sigma_1}^{\dagger}s_{\sigma_1\sigma_2}^{z}d_{i,b,\sigma_2}. \quad (41)$$

The order parameter represented by the 3×3 Hermitian matrix $\hat{D}(\hat{M})$ has nine independent components $D_{ij}(M_{ij})$. The transformation properties of these density-wave order parameters under the reflections P_xP_z and P_yP_z, inversion I, and time reversal T are summarized in Tables VI and VII. Notice that the reflections P_x and P_y are not symmetries of the system. The Hamiltonian is invariant only under the combined transformations P_xP_z and P_yP_z.

To obtain a nodal spin-density-wave ground state, we consider the simplest uniform charge-density-wave order parameter, $\hat{D}_{\mathrm{uniform}}\equiv\mathrm{diag}[d_0,d_0,d_0]$ with the finite diagonal components of $D_{11}=D_{22}=D_{33}=d_0$. This generates many Dirac points along an axis with a reflection symmetry in the momentum space, whenever a band touching occurs between two bands with opposite reflection parities. Now let us introduce another density-wave order parameter to get a gapped phase. To open a full gap between neighboring bands we need a density-wave order parameter which is odd under the reflection symmetries P_xP_z and P_yP_z. Imposing the time-reversal symmetry, the imaginary part of the spin density-wave order parameter $M_{12}^I\equiv\mathrm{Im}(M_{12})$ is the unique choice to obtain a topological insulator.

In Fig. 10(a) we plot the band structure of the uniform charge-density-wave state with nonzero $D_{\mathrm{uniform}}\neq0$ along the k_y axis. Since D_{uniform} preserves the P_xP_z reflection symmetry, each band has a definite reflection parity under P_xP_z. The reflection parities of the bands are also indicated in Fig. 10(a). Notice that nodal points exist between a pair of bands with opposite reflection parities, which are indicated by red dotted circles in Fig. 10(a). However, once we introduce a nonzero M_{12}^I, these nodal points disappear and a fully gapped phase with well-separated bands emerges. The band structure of the resulting gapped phase is described in Fig. 10(b).

To investigate the topological property of the gapped phase, we compute the spin Chern numbers of the bands. Since the z component of the spin S_z is still conserved, the spin Chern number is a well-defined quantity. In Table VIII, we show the distribution of the spin Chern numbers for several values of M_{12}^I supporting fully gapped phases. Here $C_{S,n}$ indicates the spin Chern number of the nth band defined as $C_{S,n}=N_{C,n,\uparrow}-N_{C,n,\downarrow}$, where $N_{C,n,\uparrow}(=-N_{C,n,\downarrow})$ denotes the Chern number of the nth spin-up band. We choose a labeling such that the band 1 has the highest energy and the band index n increases as the energy eigenvalue decreases. In the case of the gapped phase that is obtained by adding a small M_{12}^I on the nodal charge-density-wave state with $D_{\mathrm{uniform}}\neq0$, only the fourth and fifth band support nonzero-spin Chern numbers shown in the second column of Table VIII. Interestingly, however, as the magnitude of M_{12}^I increases, band gap closing and reopening occur successively. For instance, for the uniform density-wave state with $D_{\mathrm{uniform}}=0.5$, the first gap closing happens between the bands 1 and 2 for $M_{12}^I\approx0.15$. As M_{12}^I increases further, another fully gapped phase is obtained with the spin Chern numbers displayed in the third column of Table VIII. It is interesting to notice that after the gap closing and reopening process, the number of the bands supporting finite spin Chern numbers has increased. Similar gap closing happens again for M_{12}^I

TABLE VII. Symmetry of the spin-density order parameters with the momentum $(\pi,0)$. Here "+" ("−") indicates "even" ("odd") parity of order parameters under the corresponding symmetry operation. The complex off-diagonal components $M_{ij}(i\neq j)$ are decomposed as $M_{ij}=M_{ij}^R+iM_{ij}^I$.

	M_{11}	M_{22}	M_{33}	M_{12}^R	M_{12}^I	M_{13}^R	M_{13}^I	M_{23}^R	M_{23}^I
P_xP_z	+	+	+	−	−	−	−	+	+
P_yP_z	+	+	+	−	−	+	+	−	−
I	+	+	+	+	+	−	−	−	−
T	−	−	−	−	+	−	+	−	+

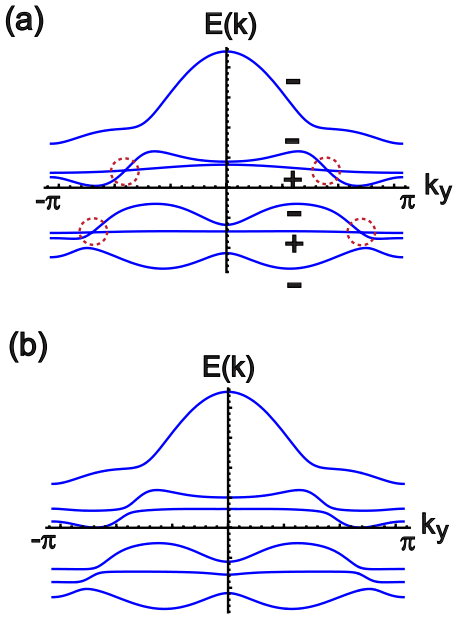

FIG. 10. (Color online) The band structures of the density-wave states with the momentum $\mathbf{k}=(\pi,0)$ along k_y axis. (a) For the uniform charge density-wave state with $D_{\text{uniform}}=0.5$. The locations of Dirac nodes are indicated by red dotted circles. The parities of the bands under the P_xP_z symmetry are indicated by + (even) and − (odd). (b) A density-wave phase with $D_{\text{uniform}}\neq 0$ and $M_{12}^I\neq 0$ at the same time. Here we take $D_{\text{uniform}}=0.5$ and $M_{12}^I=0.1$. Each band is well-separated from the other bands.

≈ 0.22 leading to the redistribution of the spin Chern numbers shown in the last column of Table VIII. Note that all cases with 1/3 filling give TDW insulators, while the TDW phase with 5/6 filling occurs only for $M_{12}^I=0.2$ and 0.3.

VII. SUMMARY AND DISCUSSION

In this paper, we investigate theoretically if topological insulators can be achieved from a nodal density-wave state with broken translational symmetry. While a nonzero density-wave order parameter in general opens a gap between the degenerate states connected by the ordering wave vector, nodal density-wave phases occur in multiorbital systems via translational symmetry breaking due to the distinct symmetry properties of orbitals. Such a nodal density-wave state supports a large number of Dirac nodes between neighboring bands. We have explicitly proved that a pair of inversion symmetric Dirac points share the same topological winding numbers in nodal density-wave states contrary to the Dirac points in the honeycomb lattice. If we introduce an additional order parameter whose transformation property under reflection symmetries is opposite to that of the underlying order parameter, the system can be a gapped insulator at certain filling factors. Among those insulators, time-reversal invariant TDW insulators with helical edge states are identified.

The existence of a nodal density-wave ground state is experimentally verified in a recent ARPES measurement on $BaFe_2As_2$ (Ref. 43) and quantum oscillation experiments on $BaFe_2As_2$ and $SrFe_2As_2$.[44–46] It is interesting to notice that, according to these experimental studies, the velocity of Dirac fermions is estimated to be 14–20 times slower than that in graphene.[46] This implies that the Dirac fermions in nodal density-wave states are more susceptible to interaction effects. However, according to our mean-field calculation, it seems to be difficult to realize quantum spin Hall insulators in Fe pnictides system, as it favors a conventional spin-density-wave state (M_0).

TABLE VIII. The spin Chern numbers of the bands for a gapped density-wave phase with $D_{\text{uniform}}\neq 0$ and $M_{12}^I\neq 0$. Here we set $D_{\text{uniform}}=0.5$ and change the magnitude of M_{12}^I.

	$M_{12}^I=0.1$	$M_{12}^I=0.2$	$M_{12}^I=0.3$
$C_{S,1}$	0	−2	−2
$C_{S,2}$	0	+2	+2
$C_{S,3}$	0	0	−4
$C_{S,4}$	−2	−2	+2
$C_{S,5}$	+2	+2	+2
$C_{S,6}$	0	0	0

Our results in general imply that transition metal materials with two-dimensional square lattice structure possessing partially filled t_{2g} orbitals are good candidates for TDW insulators. In particular, in the case of the effective two-orbital (three-orbital) model, the 1/4 filled (1/3 filled) system is the most promising for the realization of TDW insulators. However, to make a prediction on real materials with layered perovskite structure, it is important to generalize our study to three dimensional systems taking into account interlayer couplings. Stacking of two-dimensional TDW insulators simply leads to a weak topological insulator.[47] Therefore identifying three-dimensional TDW phases with a nontrivial strong topological invariant in the layered perovskite structure is an interesting but challenging future work.

Finally, it is worthwhile to comment on the emergence of spontaneous Hall conductance in a broken time-reversal symmetry state. When an imaginary charge-density-wave state (D_2) breaking time- reversal symmetry occurs in the presence of a nodal density-wave state, a gapped topological phase carries topologically protected edge modes. In contrast to the case of the quantum spin Hall insulator, here the spin-up and spin-down bands have the same Chern number, which gives rise to an insulator with finite Hall conductance. Interestingly, the imaginary charge-density-wave state is one of the competing ground states in iron-pnictide systems,[16,36,48] which is expected to be achieved in real materials.[49] Thus searching for gapped phases proximate to nodal density-wave states is an avenue to topological phases.

ACKNOWLEDGMENTS

We thank Daniel Podolsky for helpful discussions. This work was supported by the NSERC and the Canada Research Chair.

*hykee@physics.utoronto.ca

[1] X. L. Qi and S. C. Zhang, Phys. Today **63**(1), 33 (2010).
[2] J. Moore, Nature (London) **464**, 194 (2010).
[3] M. Z. Hasan and C. L. Kane, Rev. Mod. Phys. **82**, 3045 (2010).
[4] F. D. M. Haldane, Phys. Rev. Lett. **61**, 2015 (1988).
[5] C. L. Kane and E. J. Mele, Phys. Rev. Lett. **95**, 226801 (2005).
[6] H. Min, J. E. Hill, N. A. Sinitsyn, B. R. Sahu, L. Kleinman, and A. H. MacDonald, Phys. Rev. B **74**, 165310 (2006).
[7] B. A. Bernevig and S.-C. Zhang, Phys. Rev. Lett. **96**, 106802 (2006).
[8] B. A. Bernevig, T. L. Hughes, and S.-C. Zhang, Science **314**, 1757 (2006).
[9] M. König, S. Wiedmann, C. Brne, A. Roth, H. Buhmann, L. W. Molenkamp, X. L. Qi, and S. C. Zhang, Science **318**, 766 (2007).
[10] C. L. Kane and E. J. Mele, Phys. Rev. Lett. **95**, 146802 (2005).
[11] S. Raghu, X.-L. Qi, C. Honerkamp, and S. C. Zhang, Phys. Rev. Lett. **100**, 156401 (2008).
[12] Y. Ran, F. Wang, H. Zhai, A. Vishwanath, and D.-H. Lee, Phys. Rev. B **79**, 014505 (2009).
[13] M. A. H. Vozmediano, M. I. Katsnelson, and F. Guinea, Phys. Rep. **496**, 109 (2010).
[14] G. W. Semenoff, Phys. Rev. Lett. **53**, 2449 (1984).
[15] S. Raghu, X.-L. Qi, C.-X. Liu, D. J. Scalapino, and S.-C. Zhang, Phys. Rev. B **77**, 220503(R) (2008).
[16] A. V. Chubukov, D. V. Efremov, and I. Eremin, Phys. Rev. B **78**, 134512 (2008).
[17] We choose $\mathbf{Q}=(\pi,0)$ for simplicity but the general criteria for obtaining TDW phase do not depend on the choice of $\mathbf{Q}$.
[18] K. Sun and E. Fradkin, Phys. Rev. B **78**, 245122 (2008).
[19] K. Sun, H. Yao, E. Fradkin, and S. A. Kivelson, Phys. Rev. Lett. **103**, 046811 (2009).
[20] Y. D. Chong, X.-G. Wen, and M. Soljacic, Phys. Rev. B **77**, 235125 (2008).
[21] O. Vafek and K. Yang, Phys. Rev. B **81**, 041401(R) (2010).
[22] X.-L. Qi, S. Raugh, C.-X. Liu, D. J. Scalapino, and S.-C. Zhang, arXiv:0804.4332 (unpublished).
[23] M. Onoda and N. Nagaosa, J. Phys. Soc. Jpn. **71**, 19 (2002).
[24] X.-L. Qi, Y.-S. Wu, and S.-C. Zhang, Phys. Rev. B **74**, 085308 (2006).
[25] D. N. Sheng, Z. Y. Weng, L. Sheng, and F. D. M. Haldane, Phys. Rev. Lett. **97**, 036808 (2006).
[26] L. Fu and C. L. Kane, Phys. Rev. B **74**, 195312 (2006).
[27] D. J. Thouless, M. Kohmoto, M. P. Nightingale, and M. den Nijs, Phys. Rev. Lett. **49**, 405 (1982).
[28] M. Kohmoto, Ann. Phys. (N.Y.) **160**, 343 (1985).
[29] N. Nagaosa, J. Phys. Soc. Jpn. **75**, 042001 (2006).
[30] M. Koenig, H. Buhmann, L. W. Molenkamp, T. L. Hughes, C.-X. Liu, X.-L. Qi, and S.-C. Zhang, J. Phys. Soc. Jpn. **77**, 031007 (2008).
[31] A. N. Redlich, Phys. Rev. D **29**, 2366 (1984).
[32] T. Fukui and Y. Hatsugai, Phys. Rev. B **75**, 121403 (2007).
[33] L. Fu and C. L. Kane, Phys. Rev. B **76**, 045302 (2007).
[34] G. E. Volovik, Lect. Notes. Phys **718**, 31 (2007).
[35] F. Wang, H. Zhai, Y. Ran, A. Vishwanath, and D.-H. Lee, Phys. Rev. Lett. **102**, 047005 (2009).
[36] H. Zhai, F. Wang, and D.-H. Lee, Phys. Rev. B **80**, 064517 (2009).
[37] J. Merino, H. Seo, and M. Ogata, Phys. Rev. B **71**, 125111 (2005).
[38] M. Daghofer, A. Nicholson, A. Moreo, and E. Dagotto, Phys. Rev. B **81**, 014511 (2010).
[39] P. A. Lee and X.-G. Wen, Phys. Rev. B **78**, 144517 (2008).
[40] S. Graser, T. A. Maier, P. J. Hirschfeld, and D. J. Scalapino, New J. Phys. **11**, 025016 (2009).
[41] K. Kuroki, S. Onari, R. Arita, H. Usui, Y. Tanaka, H. Kontani, and H. Aoki, Phys. Rev. Lett. **101**, 087004 (2008).
[42] In Ref. 38, t_8 and t_7 was fixed by $t_8=-t_7/2$ to make the electron pockets have pure xy character along $\Gamma-X$ and $\Gamma-Y$ directions. Since this additional constraint generates accidental band crossing points, we introduce 10% modulation in the magnitude of t_8, which does not affect the overall band structure and the shape of the Fermi surfaces.
[43] P. Richard, K. Nakayama, T. Sato, M. Neupane, Y.-M. Xu, J. H. Bowen, G. F. Chen, J. L. Luo, N. L. Wang, X. Dai, Z. Fang, H. Ding, and T. Takahashi, Phys. Rev. Lett. **104**, 137001 (2010).
[44] S. E. Sebastian, J. Gillet, N. Harrison, P. H. C. Lau, D. J. Singh, C. H. Mielke, and G. G. Lonzarich, J. Phys.: Condens. Matter **20**, 422203 (2008).
[45] J. G. Analytis, R. D. McDonald, J.-H. Chu, S. C. Riggs, A. F. Bangura, C. Kucharczyk, M. Johannes, and I. R. Fisher, Phys. Rev. B **80**, 064507 (2009).
[46] N. Harrison and S. E. Sebastian, Phys. Rev. B **80**, 224512 (2009).
[47] L. Fu, C. L. Kane, and E. J. Mele, Phys. Rev. Lett. **98**, 106803 (2007).
[48] D. Podolsky, H.-Y. Kee, and Y. B. Kim, Europhys. Lett. **88**, 17004 (2009).
[49] Z.-J. Yao, J.-X. Li, Q. Han, and Z. D. Wang, arXiv:1003.1660 (unpublished).